Geochemistry, Geophysics, Geosystems

RESEARCH ARTICLE
10.1029/2020GC009577

Is There a Speed Limit for the Thermal Steady-State Assumption in Continental Rifts?

Esther L. Heckenbach[1,2], Sascha Brune[1,2], Anne C. Glerum[1], and Judith Bott[1]

[1]GFZ German Research Centre for Geosciences, Potsdam, Germany, [2]Institute of Geosciences, University of Potsdam, Potsdam-Golm, Germany

Key Points:

- We use numerical forward modeling to quantify the transient thermal imprint of continental extension
- The validity of the thermal steady-state assumption in narrow rifts is limited to extension velocities less than 0.5–2 mm/a
- Transient thermal effects are particularly significant for deep isotherms, narrow rifts, and beneath the rift shoulders

Supporting Information:

- Supporting Information S1

Correspondence to:
E. L. Heckenbach,
hecken@gfz-potsdam.de

Citation:
Heckenbach, E. L., Brune, S., Glerum, A. C., & Bott, J. (2021). Is there a speed limit for the thermal steady-state assumption in continental rifts? *Geochemistry, Geophysics, Geosystems*, *22*, e2020GC009577. https://doi.org/10.1029/2020GC009577

Received 1 DEC 2020
Accepted 11 FEB 2021

Abstract The lithosphere is often assumed to reside in a thermal steady-state when quantitatively describing the temperature distribution in continental interiors and sedimentary basins, but also at active plate boundaries. Here, we investigate the applicability limit of this assumption at slowly deforming continental rifts. To this aim, we assess the tectonic thermal imprint in numerical experiments that cover a range of realistic rift configurations. For each model scenario, the deviation from thermal equilibrium is evaluated. This is done by comparing the transient temperature field of every model to a corresponding steady-state model with an identical structural configuration. We find that the validity of the thermal steady-state assumption strongly depends on rift type, divergence velocity, sampling location, and depth within the rift. Maximum differences between transient and steady-state models occur in narrow rifts, at the rift sides, and if the extension rate exceeds 0.5–2 mm/a. Wide rifts, however, reside close to thermal steady-state even for high extension velocities. The transient imprint of rifting appears to be overall negligible for shallow isotherms with a temperature less than 100°C. Contrarily, a steady-state treatment of deep crustal isotherms leads to an underestimation of crustal temperatures, especially for narrow rift settings. Thus, not only relatively fast rifts like the Gulf of Corinth, Red Sea, and Main Ethiopian Rift, but even slow rifts like the Kenya Rift, Rhine Graben, and Rio Grande Rift must be expected to feature a pronounced transient component in the temperature field and to therefore violate the thermal steady-state assumption for deeper crustal isotherms.

Plain Language Summary Temperature distribution is a key factor when studying Earth's interior. Here, we quantify the influence of rift velocity on temperature distribution with numerical simulations. As a continent begins to split, forming a rift, hot material beneath the rift center moves upwards increasing the temperatures at shallow crustal depth. However, simple thermal models often assume an equilibrated, constant temperature field. To evaluate tectonically induced changes in temperatures, we compare lithosphere-scale dynamic models to models with the same material configuration but with a steady-state temperature distribution and no deformation. We find that the latter approach well represents locations outside the rift valley and shallow crustal depths where comparably low temperatures prevail. Contrarily, at the sides of the rift valley, or for deeper-lying isotherms like 400°C, the assumption of an equilibrated thermal field leads to an underestimation of crustal temperatures. Furthermore, we show that temperatures in narrow rifts like the Kenya Rift and the Rhine Graben are more strongly modified by tectonic movements than temperatures in wide rifts, like the Basin and Range Province. Finally, we conclude that the assumption of constant temperatures is only valid for wide rifts and very slowly extending narrow rifts with a speed limit of <0.5–2 mm/a.

1. Introduction

The temperature distribution within the lithosphere exerts key control on major geological and geodynamic processes such as long-term tectonic deformation, seismicity, and geochemical reactions. To better understand the localization of deformation, for instance, one may describe the thermo-mechanical state of the lithosphere (Afonso & Ranalli, 2004; Burov, 2011) in order to numerically simulate forward tectonic deformation (e.g., Buck, 1991; Huismans et al., 2005). Additional to these fundamental processes, shallow crustal temperatures hold strong implications for applied research on the formation of georesources. For example, the depth of the 60°C and the 120°C isotherms are important indicators for a region's geothermal potential in terms of heat production and electricity, respectively (e.g., Gudmundsson, 1988), while the depth of the oil window (80°C–100°C) (e.g., Tissot et al., 1987) controls the sites of hydrocarbon formation. The thermal

evolution of tectonically active regions may be reconstructed using thermochronological techniques, which in turn require the present-day temperature distribution as a key constraint. Hence, quantifying the present-day thermal field of the sediments, crust, and lithospheric mantle is of profound relevance for a variety of applied and fundamental research problems.

Deducing the temperature distribution within sedimentary basins is an immense challenge, because borehole-derived subsurface temperatures and surface heat flow measurements are notoriously sparse compared to the dimensions of sedimentary basins. Hence, for the gapless assessment of present-day thermal field variations in a region, the scientific community reverts to a variety of predictive models that range from purely mathematical approaches (interpolation algorithms ignoring geological structure; e.g., Agemar et al., 2014) to heat transport simulations that take into account lithology controlled thermal property variations. The latter type of models typically considers how efficiently the rocks at depth conduct heat (since solid-state heat diffusion is the main heat transport process in the lithosphere; Scheck-Wenderoth et al., 2014), how much heat is produced by radioactive decay, and how much heat is transferred across the external boundaries of the modeled system. Hence, the setup of such models involves an extensive analysis of observational data (e.g., wells, seismic profiles, and gravity anomalies) to integrate the subsurface geological structure, rock types, related thermal properties, and appropriate boundary conditions. Thereby, the amount of heat entering the system from the mantle has to be defined at the lower boundary, which implies that the models are at least crustal or even lithospheric in scale (e.g., Balling et al., 2013; Bayer et al., 1997; Carballo et al., 2015; Freymark et al., 2017; Fullea et al., 2012, 2009; Jiménez-Munt et al., 2019; Maystrenko & Gernigon, 2018; Sippel et al., 2017; Tesauro et al., 2009). In the frame of this study, we refer to these regional-scale heat transport simulations as data-integrative thermal models.

Even if this type of models may be reasonably accurate in terms of the subsurface configuration of rock properties, there is one crucial assumption they are based on, which may not be valid everywhere: Heat is assumed to be transported within an instantaneously thermally equilibrated lithosphere. In other words, these models assume a thermal steady-state condition where temperature does not change through time. A thermal steady-state, however, is in contradiction to many active tectonic settings where transient processes are well-known to play a role. This has been shown, for example, by the misfits of steady-state thermal models with respect to measured temperature data, which have been interpreted to result from transient thermal processes as the remnants of the thermal evolution within the study region (e.g., Freymark et al., 2017; Fullea et al., 2012; Meeβen, 2019). Indeed, the transient nature of lithospheric temperature signals is a common problem (e.g., Artemieva, 2009; Balling et al., 2013; Tesauro et al., 2009) and can be expected in a variety of timescales affecting different depths of the lithosphere. This includes comparably shallow signals that arise from paleoclimate effects (e.g., Heckenbach et al., 2019; Lane, 1923) as well as lithospheric-scale perturbations related to the tectonic evolution (e.g., Artemieva, 2009; Chenin et al., 2020; Peacock, 1996; Smye et al., 2019). Transient perturbations of the thermal field should hence be mainly expected in active plate boundary settings where tectonic deformation, heat advection, and changing heat source distributions would generate time-dependent temperature fields (e.g., Davies et al., 2016; Ehlers & Farley, 2003; Hart et al., 2017).

In this study, we focus on currently active continental rifts as an example of actively deforming plate boundaries (see Figure 1 and Table 1). Continental rifts form where divergent lateral motions thin the lithosphere. This causes the lithosphere-asthenosphere boundary (LAB) to move upwards and hot material to be advected to shallower depths. Rifts can generally be categorized into narrow and wide rifts: Narrow rifts feature pronounced rift valleys less than 100 km wide, as in large parts of the East African Rift System (Ebinger & Scholz, 2012) or the Rhine graben (Brun et al., 1992), while wide rifts are characterized by several smaller horsts and grabens distributed over a larger area, as for example, the Basin and Range Province or the Aegean (Brun & Sokoutis, 2018; Hamilton, 1987; Rey et al., 2009). Numerical thermo-mechanical simulations show that narrow rifts form in strong crustal configurations, while deformation in wide rifts is less localized due to a weaker crust and associated crust-mantle decoupling (Buck, 1991).

Here we perform a quantitative assessment of the systematic variations of tectonically induced thermal transients in narrow and wide rift settings. To this aim, we employ 2D thermo-mechanical forward models that account for visco-plastic deformation of the lithosphere, conductive and advective heat transport as well as heat generation due to radiogenic decay and shear heating. These models reproduce the time-dependent

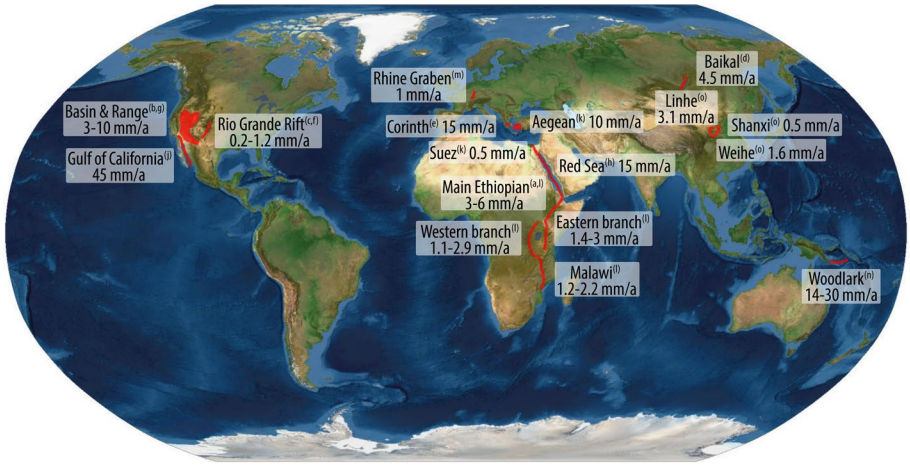

Figure 1. Locations of active continental rifts with their extension velocities. More information on the individual rifts is given in Table 1, including references (indicated here by superscripts).

Table 1
Active Rifts of the World With Their Extension Velocities and the Type of Data Used to Determine Velocities

Rift name	$v_{extension}$ [mm/a]	Data used to constrain $v_{extension}$	Reference
Aegean	10	Geodesy	(k) Reilinger et al. (2010)
Baikal	4.5	Geodesy	(d) Calais et al. (1998)[a]
Basin and Range—Walker Lane Fault Region	10	Geodesy	(b) Bennett et al. (1998); Hammond and Thatcher (2004)[a]
Basin and Range—Wasatch Fault Zone	3	Geodesy	(g) Kreemer et al. (2010)[a]
EARS—Eastern branch	1.4–3	Best fit model (GPS + Geology + EQ)	(l) Saria et al. (2014)
EARS—Western branch	1.1–2.9	Best fit model (GPS + Geology + EQ)	(l) Saria et al. (2014)
Gulf of California	44 (60–70° obliquity)	Correlating Miocene volcanic strata	(j) Oskin et al. (2001) in McQuarrie and Wernicke (2005), Brune (2014)
Gulf of Corinth	15	Geodesy	(e) Gawthorpe et al. (2018) and references therein
Linhe (Hetao Graben)	3.1	Geological reconstruction (2.4 Ma)	(o) Zhang et al. (1998)
Main Ethiopian Rift	3–6	Geodesy	(a) Bendick et al. (2006); Kogan et al. (2012)[a]
	5	Best fit model (GPS + Geology + EQ)	(l) Saria et al. (2014)
Malawi Rift	1.2–2.2	Best fit model (GPS + Geology + EQ)	(l) Saria et al. (2014)
Red Sea Rift	15	Geodesy	(h) McClusky et al. (2010)[a]
Rhine Graben	1	Geodesy	(m) Tesauro et al. (2005)
Rio Grande Rift	1.2	Geodesy (4 years)	(c) Berglund et al. (2012)[a]
	0.2	Geological reconstruction (26 Ma)	(f) Golombek et al. (1983)[a]
Shanxi	0.5	Geological reconstruction (2.4 Ma)	(o) Zhang et al. (1998)
Suez	0.5	Geodesy	(k) Reilinger et al. (2010)
Weihe	1.6	Geological reconstruction (2.4 Ma)	(o) Zhang et al. (1998)
Woodlark	14–30	Geodesy	(n) Tregoning et al. (1998)

Notes. Locations are shown in Figure 1. EARS: East African Rift System, $v_{extension}$: extension velocity, EQ: earthquake slip vector data, GPS: velocities measured using the Global Positioning System.
[a]from Tetreault and Buiter (2018).

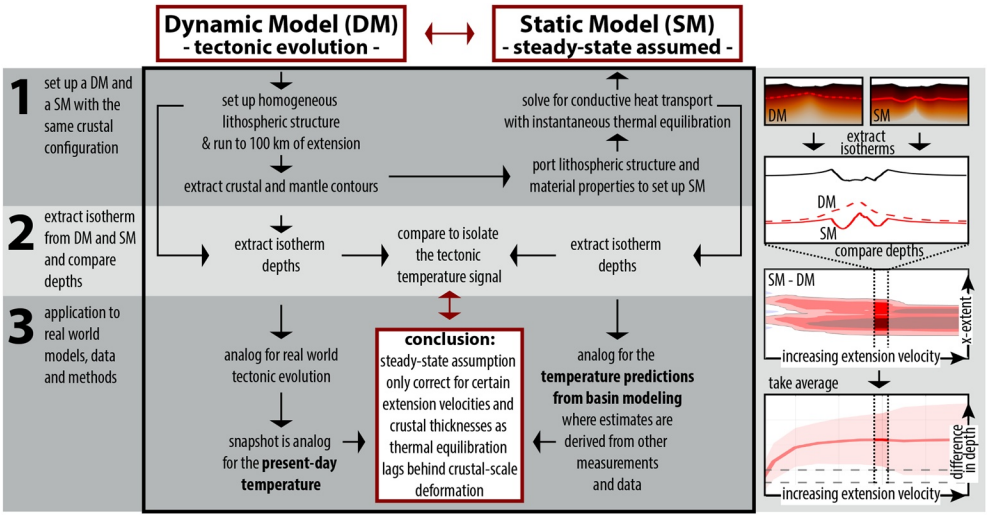

Figure 2. Graphical summary of the workflow used to assess the meaningfulness of a steady-state thermal modeling approach by comparing time-dependent dynamic (DM) and static models that assume a steady-state temperature distribution (SM).

evolution of rift structures and the resulting thermal field on a lithospheric scale. The central approach of this study is to isolate the transient tectonic component of the temperature distribution from each model run. This is done by quantifying, for each time step, the temperature differences to the steady-state thermal field that would be associated with the structural configuration of this particular time step (Figure 2). Ultimately, this allows us to investigate the dependence of the transient temperature component on rift divergence velocity and to deduce general applicability limits for the thermal steady-state assumption in continental rifts.

With this paper we intend to provide: (1) a systematic overview of the sensitivity of thermal transients to extension rates and to the initial crustal configuration; and (2) a framework to assess, for any particular rift of known extension velocity and crustal geometry, the meaningfulness of a steady-state thermal modeling approach that neglects tectonically induced transient signals.

2. Methods

The relation between the validity of the thermal steady-state assumption and the extension velocity of continental rifts is assessed by evaluating 44 2D box models. In this section, we first state the governing equations of our numerical software. We then describe the setup of the thermo-mechanical forward models that compute the evolution of the transient temperature field. Last, we introduce the static models where we solve for the steady-state temperature distribution for a given lithospheric configuration. The entire workflow is furthermore graphically summarized in Figure 2.

All numerical modeling is carried out using the finite element geodynamic code ASPECT (Bangerth et al., 2018; Heister et al., 2017; Kronbichler et al., 2012; Rose et al., 2017). In this study, it solves the incompressible flow equations of momentum, mass and energy (assuming an infinite Prandtl number) for velocity $\boldsymbol{v}$, pressure P, and temperature T, combined with advection equations for each Eulerian compositional field c_i:

$$-\nabla \cdot \left(2\eta\dot{\epsilon}\right) + \nabla P = \rho \mathbf{g} \tag{1}$$

$$\nabla \cdot \mathbf{v} = 0 \tag{2}$$

Table 2
Material Properties Used in the Dynamic and Steady-state Models

	Upper crust (Wet quartzite)	Lower crust (Wet anorthite)	Lithospheric mantle and asthenosphere (Dry olivine)	Unit
Thermal properties				
Thermal diffusivity κ	0.772	0.731	0.838	$mm^2\ s^{-1}$
Heat capacity c_p	1,200	1,200	1,200	$J\ kg^{-1}\ K^{-1}$
Density ρ	2,700	2,850	3,280	$kg\ m^{-3}$
Thermal expansivity α	2.70	2.70	3.00	$10^{-5}\ K^{-1}$
Radioactive heating H	1.5	0.2	0	$\mu W\ m^{-3}$
Dislocation creep	([a])	([b])	([c])	
Prefactor A_{ds}	8.57×10^{-28}	7.13×10^{-18}	6.54×10^{-16}	$Pa^{-n}\ s^{-1}$
Stress exponent n_{ds}	4	3	3.5	-
Activation energy E_{ds}	223	345	530	$kJ\ mol^{-1}$
Activation volume V_{ds}	0	3.80×10^{-5}	1.80×10^{-5}	$cm^3\ mol^{-1}$
Diffusion creep	([a])	([b])	([c])	
Prefactor A_{df}	5.97×10^{-19}	2.99×10^{-25}	2.25×10^{-9}	$Pa^{-1}\ s^{-1}$
Grain size exponent m_{df}	2	3	0	-
Activation energy E_{df}	223	159	375	$kJ\ mol^{-1}$
Activation volume V_{df}	0	3.80×10^{-5}	6.00×10^{-6}	$cm^3\ mol^{-1}$
Drucker-Prager plasticity				
Unweakened friction angle ϕ	26.56	26.56	26.56	°
Cohesion C	20	20	20	MPa

Note. Reference temperature $T_0 = 293$ K, grain size $d = 1e{-}3$, the user-defined minimum and maximum viscosities are $\eta_{min} = 1e17$ and $\eta_{max} = 1e24$. Frictional strain weakening is implemented by a linear reduction of the friction angle between strains of 0 and 0.5 by up to 90%.
[a]Rutter and Brodie (2004). [b]Rybacki et al. (2006). [c]Hirth and Kohlstedt (2004).

$$\bar{\rho} c_P \left(\frac{\partial T}{\partial t} + \mathbf{v} \cdot \nabla T \right) - \nabla \cdot k \nabla T = \bar{\rho} H \text{ radioactive heating} + (2\eta\ \dot{\epsilon}) : \dot{\epsilon} \text{ shear heating} + \alpha T (\mathbf{v} \cdot \nabla P) \text{adiabatic heating} \tag{3}$$

$$\frac{\partial c_i}{\partial t} + \mathbf{v} \cdot \nabla c_i = 0, \tag{4}$$

where η is the effective viscosity (see Equations 5–8), $\dot{\epsilon}$ is the deviator of the strain rate tensor $\frac{1}{2}(\nabla \mathbf{v} + (\nabla \mathbf{v})^T)$, density $\rho = \rho_0(1 - \alpha(T - T_0))$ with T_0 the reference temperature, and $\mathbf{g}$ gravity. $\bar{\rho}$ is the adiabatic reference density, c_P the specific isobaric heat capacity, k the thermal conductivity, and α the thermal expansivity, as given in Table 2. ASPECT is based on state-of-the-art numerical methods (Arndt et al., 2017), and we make use of a wide range of functionalities including nonlinear rheologies, free surface, adaptive time-stepping, mesh refinement and high performance iterative solvers (Bangerth et al., 2018; Heister et al., 2017; Kronbichler et al., 2012; Rose et al., 2017).

The initial model domain of the dynamic models is 500 km wide and 125 km deep. Three steps of initial mesh refinement in the central rectangular areas shown in Figure 3 result in an effective resolution of 250 m in the rift area and a resolution of 2 km in the asthenosphere. The model includes four material layers (upper crust, lower crust, lithospheric mantle, and asthenosphere) with different compositions (Figure 3,

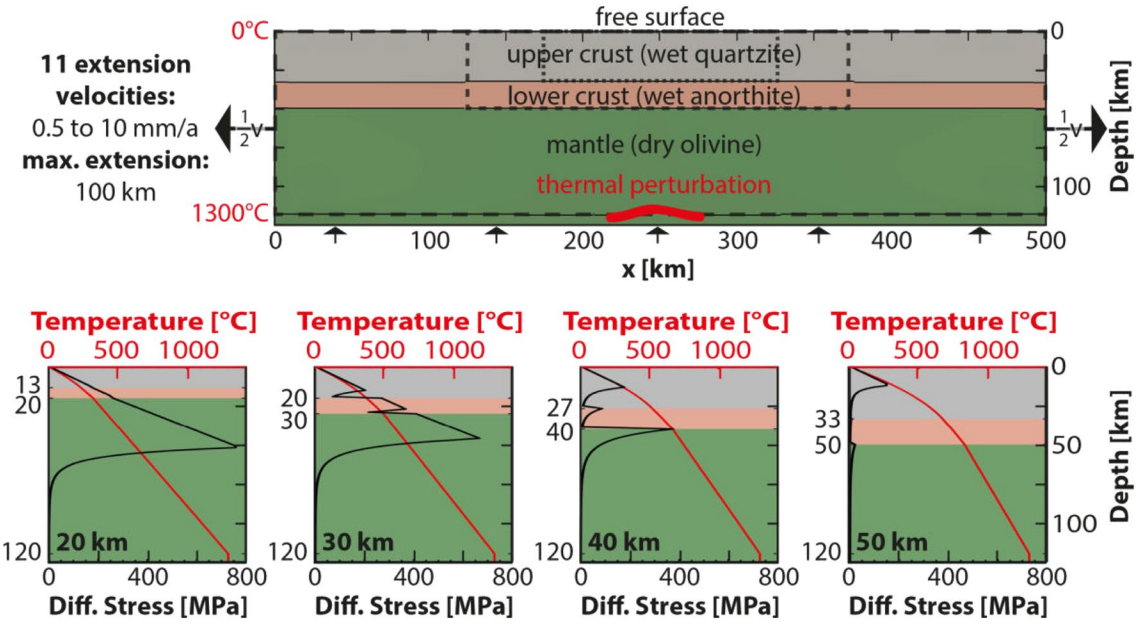

Figure 3. Top: Composition and initial geometry of the lithosphere with four horizontal layers and a thermal and compositional perturbation of the lithosphere-asthenosphere boundary (LAB). For the initial temperature field, we prescribe adiabatic conditions in the asthenosphere and a conductive temperature profile in the lithosphere (Equation 10) that is bounded by 0°C at the surface and 1300°C at the bottom of the lithosphere. The boundary conditions for the governing equations are a fixed composition at the bottom boundary, and a fixed temperature at the top and bottom boundary. Furthermore, the top boundary is a free surface, while the sides and bottom boundaries have prescribed velocities in boundary-perpendicular directions. The mesh-refined areas are framed with dashed lines with decreasing dash size indicating smaller element sizes of up to 250 m of resolution at the central surface compared to 2 km in the asthenosphere. **Bottom:** Initial temperature and yield strength profiles for the four crustal thicknesses that we considered.

Table 2). Except for the LAB, where a small perturbation is included in the model center, the layers are initially horizontal. We vary total crustal thickness, but for simplicity the upper crust is always chosen twice as thick as the lower crust. A thermal LAB is implemented at 120 km depth for all models (Figure 3), corresponding to a lithosphere thickness representative of typical intraplate environments (Artemieva, 2006). Initial temperature profiles are calculated with the boundary conditions of 0°C at the surface and 1300°C at the LAB assuming conductive heat transport and radioactive heating within an instantaneously equilibrated lithosphere (Equation 10) and adiabatic conditions within the asthenosphere (Turcotte & Schubert, 2014). The adiabatic surface temperature is set to 1284°C.

We employ a visco-plastic rheology (Glerum et al., 2018) with dislocation and diffusion creep rheologies as well as the Drucker–Prager yield criterion. In 2D, these are incorporated within ASPECT through the following equations:

$$\eta_{eff}^{comp} = \left(\frac{1}{\eta^{df}} + \frac{1}{\eta^{ds}}\right)^{-1} \quad \text{composite viscosity} \tag{5}$$

$$\text{with} \quad \eta_{ds\backslash df} = \frac{1}{2} A^{-\frac{1}{n_{ds\backslash df}}} d^{\frac{m_{ds\backslash df}}{n_{ds\backslash df}}} \dot{\epsilon}_{ii}^{\frac{1-n_{ds\backslash df}}{n_{ds\backslash df}}} exp\left(\frac{E_{ds\backslash df} + PV_{ds\backslash df}}{n_{ds\backslash df} RT}\right) \quad \text{ds | df creep} \tag{6}$$

When $2\eta_{eff}^{comp}\dot{\epsilon} > \sigma_y$, the plastic effective viscosity ($Eq.\ 7$) is used instead of the composite effective viscosity (Eq.5):

$$\eta_{eff}^{pl} = \frac{\sigma_y}{2\dot{\epsilon}_{ii}} \quad \text{plastic effective viscosity} \tag{7}$$

with

$$\sigma_y = P \cdot \sin(\phi) + C \cdot \cos(\phi) \quad \text{Drucker - Prager plasticity} \tag{8}$$

where η_{eff} is the effective viscosity, $ds|df$ corresponds to dislocation or diffusion creep, d is grain size, R is the gas constant, $A_{\text{ds|df}}$ are prefactors, $n_{\text{ds|df}}$ and $m_{\text{ds|df}}$ are stress and grain size exponents. For diffusion creep, $n_{\text{df}} = 1$, while for dislocation creep, $m_{\text{ds}} = 0$. $E_{\text{ds|df}}$ are the activation energies, $V_{\text{ds|df}}$ are the activation volumes, σ_y is the yield stress, ϕ is the internal angle of friction and C is cohesion. $\dot{\epsilon}_{ii}$ is defined as the square root of the second invariant of the deviatoric strain rate tensor. The final effective viscosity (Equations 5 and 7) is capped by a user-defined minimum and maximum viscosity η_{min} and η_{max}. All parameters are listed in Table 2.

Rift localization is facilitated by a thermal and compositional perturbation in the center of the model where the LAB is elevated maximally by 5 km using a Gaussian distribution with a half-width of 10 km (Brune et al., 2014). Furthermore, the initial strain field is constructed using random noise with a Gaussian distribution around the domain center of which the standard deviation is 200 km and the maximum amplitude is 0.2. The initial strain is smoothed out at 50 km depth. This results in a random distribution in terms of lateral heterogeneity of modeled friction angles through linear strain weakening on the plastic strain interval [0–0.5], reflecting the nonhomogeneity of natural rocks and facilitating the localization of deformation (Duclaux et al., 2018; Jammes & Lavier, 2016; Naliboff et al., 2017).

The top boundary is a free surface (Rose et al., 2017) allowing for topography to evolve throughout the extension process, while material velocities are prescribed for all other boundaries with the bottom inflow matching the outflow through the sides (Figure 3). Prescribing divergent velocities at model boundaries represents a wide range of driving forces of rifting, such as (1) plate divergence that is driven by large-scale mantle drag beneath the involved plates (Ulvrova et al., 2019), (2) back-arc extension due to slab-dynamics induced trench retreat (Sdrolias & Müller, 2006), and (3) rifting that is caused by plume-related gravitational potential energy gradients on a wavelength of thousands of kilometers (Kendall & Lithgow-Bertelloni, 2016; Stamps et al., 2010). Each of these processes affects the ~100 km wide plate boundary primarily through divergent plate motion, which we approximate by prescribing velocities at the model boundaries. Model properties like temperature, pressure, stress, and strain fields are output every 2 km of applied extension. Models are stopped when 100 km of accumulated total extension is reached. The dynamic model suite includes 11 rift velocities (0.5,1,2,...,10 mm/a) and four crustal thicknesses (20, 30, 40, 50 km). We therewith cover the majority of modern rifts worldwide (Figure 1 and Table 1).

Further understanding of the dominant modeled processes is gained by calculating the Péclet number (Pe) for each model setup, which describes the ratio of conductive to advective heat transport. A small Péclet number ($Pe < 1$) indicates a predominantly conductive setting, while a large Péclet number ($Pe > 1$) designates dominantly advective heat transport (Sandiford, 2002). We calculate a Péclet number for each rift setting with:

$$Pe = \frac{L \cdot v}{\kappa} \tag{9}$$

According to Guillou-Frottier et al. (1995), where L is the initial thickness of the lithosphere [km], v is the prescribed vertical inflow velocity [mm a^{-1}] and κ is the thermal diffusivity [m^2 a^{-1}].

Contrary to the dynamic models that capture the entire rift evolution, our models assuming thermal steady-state only represent snapshots in time and hence do not include the tectonically inherited transient temperature field, nor any additional thermal perturbations. To ensure applicability of the results, the construction of these models is done in correspondence to the approach of data-integrative thermostructural models. These data-integrative models first generate a structural model of the area based on topography, gravity, seismic, and borehole data, which then serves as the framework for the modeling of the thermal field

(Balling et al., 2013; Jiménez-Munt et al., 2019; Sippel et al., 2017). Analogous to this approach, we first extract the structural setting that is specific for a given time step of extension from the dynamic models, that is, the material contours and model surface at the time when 50 km of extension has accumulated. We then use these structural interfaces to initialize a new set of models without deformation, where the thermal field is composed of 1D vertical profiles that are calculated by solving the 1D steady-state heat equation (Chapman, 1986; Turcotte & Schubert, 2014)

$$0 = \kappa \frac{\partial^2 T}{\partial z^2} + \frac{H}{c_p} \tag{10}$$

where κ is the bulk thermal diffusivity [$m^2\ s^{-1}$], T is the temperature [K], H is the radiogenic heat production [$W\ m^{-3}$] and c_p is the heat capacity [$J\ K^{-1}$]. The steady-state temperature field hence entirely depends on the material properties κ, H and c_P of the three compositional layers (Table 2) and the assumption of conductive heat flow that leads to an instantaneous equilibration of the thermal field between the boundary conditions of 1300°C at the LAB and 0°C at the surface.

3. Results

In this section, we first present the outcome of the evolution of the dynamic models, which provide the structural setup for the steady-state models. We describe the general rift evolution patterns of the dynamic models, before we focus on the temperature distribution and compare it to the thermal fields of the steady-state models. Finally, we introduce a threshold value to quantitatively assess the validity of thermal steady-state models in the light of extension velocity.

Our dynamic models reproduce first-order rift characteristics, such as lithospheric thinning accommodated by crustal faulting and ductile shear zone formation at depth. They show foot wall uplift and hanging wall subsidence with pronounced basin formation for narrow rift scenarios. The highest topography contrasts emerge in models with the thinnest crust, as expected from classical studies (Braun & Beaumont, 1989; Buck, 1991). The development of dominant border faults and the migration of fault activity toward the center of the rift matches geologic observations, for example, from the East African Rift System (Corti et al., 2018; Ebinger & Scholz, 2012). The formation of major shear zones in the lower crust and upper mantle is supported by a range of published rift models (Duretz et al., 2016; Huismans & Beaumont, 2003; Pourhiet et al., 2004).

In agreement with further previous numerical studies, we find that crustal thickness and therefore crustal strength are the key parameters affecting whether narrow or wide rifts are formed (Armitage et al., 2018; Brune et al., 2017; Tetreault & Buiter, 2018): Models with 20–30 km thick crust generate distinct, ~70 km wide half grabens within a few million years that develop into asymmetric narrow rifts (Figure 3). Over the modeled period, the rift valley reaches a width of about 180 km and the crust is thinned to only a few kilometers within the central parts of the rift. In models with thicker crust (40–50 km), however, deformation takes more time to localize and a wide rift evolves with strain and topography being distributed over the entire model domain. In this case, the material layers of the model are thinned more homogeneously over the width of the model due to the formation of several, roughly equally spaced rift faults.

Based on this consistent structural evolution, we evaluate the temperature distribution in the crust. The temperature field of the dynamic models is affected by conduction and advection of heat, as well as heat generation due to radiogenic, adiabatic, and shear heating. The interplay of these processes generates a thermal field of a complex transient nature (Figures 4a and 5a). Contrarily, in the steady-state models, the temperature field is only affected by heat conduction and radiogenic heating. This results in relatively evenly spaced isotherms for each 1D profile along the modeled sections (Figures 4b and 5b). It also leads to a strong influence of the surface topography on the geometry of shallow isotherms like the 100°C, while the deeper isotherms mimic the shape of the LAB. A strong impact of the LAB can be observed even for intermediate temperatures like the 400°C isotherm. Resulting amplitudes in the topography of the isotherms are distinctly larger in narrow rift models with 20–30 km of initial crustal thickness than in wide rift settings with 40–50 km of initial crustal thickness (Figures 4a, 4b, 5a, and 5b). In Figure S6 we show that the strong influence of the surface topography and the LAB on the shape of the isotherms can be avoided by using a 2D

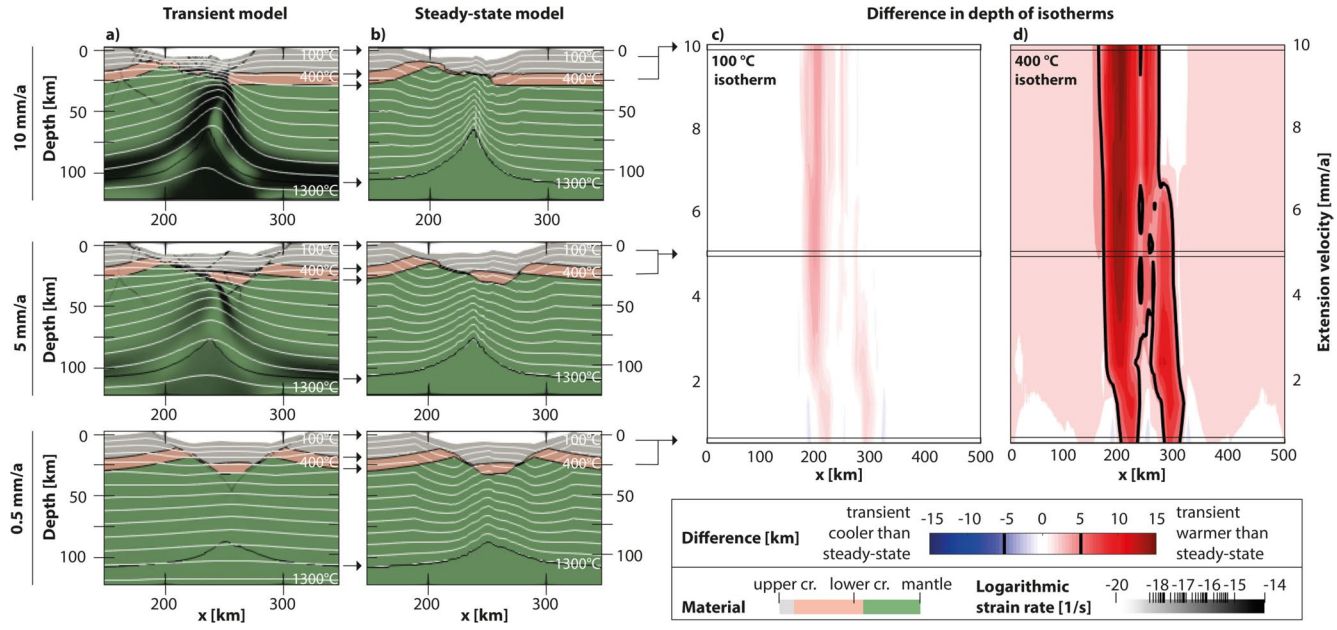

Figure 4. Left: Profiles of three exemplary **narrow rift models** with an initial crustal thickness of 30 km and different extension velocities (of 0.5, 5 and 10 mm/a, respectively). (a) The thermal, compositional, and deformation structure of the transient model at 50 km of total extension and (b) the corresponding steady-state model. Colors indicate the different materials of the model as given in Figure 3 and Table 2. The strain rate is superposed in a transparent gray scale. White lines mark the depths of isotherms with a spacing of 100°C. Black arrows between (a) and (b) point at the material contours that are extracted from the transient models to define the material structure of the steady-state models. **Right:** Influence of the extension velocity on the difference between transient and steady-state models. Differences between transient and steady-state models are color-coded in terms of the respective $\Delta d_{\text{isotherm}}$ of (c) the 100°C isotherm and (d) the 400°C isotherm. Red colors indicate a warmer crust in the transient model with the isotherms being shallower compared to the steady-state model. The black contour marks a 5 km difference in depth.

thermal steady-state approach (see supplement for methodology). The results for the exemplary 2D steady-state model demonstrate that the small scale variability of the depth difference is smoothed out for models employing a 2D thermal steady-state compared to those using 1D thermal steady-state computations. However, the magnitude and spatial distribution remains comparable for both approaches.

The comparison between transient and steady-state model temperatures shows that shallow, crustal isotherms predicted by steady-state models are generally deeper than those from the corresponding transient models (compare Figures 4b and 5b to Figures 4a and 5a). To a small degree, this effect is caused by shear heating that releases heat in areas of active faulting. However, the key control on this effect can be understood when considering that the dynamic models feature a pronounced vertical advection component that is not represented in the steady-state models. In order to further explore the impact of heat advection, we explicitly compare the depth of a shallow and a deep crustal isotherm (100°C and 400°C, respectively) between transient and corresponding steady-state models (Figures 4c, 4d, 5c, and 5d—results for more isotherms up to 600°C are shown in the Figures S5a and S5b). These two isotherms provide a characteristic representation of the temperature spectrum relevant for georesources and geochronological applications. For example, the closure temperature for fission tracks in apatite is ~100°C and ~300°C in zircon (Braun et al., 2006). Isotherm depths are extracted from both the transient and the steady-state models over the entire width of the model domain and are then compared by subtracting one depth from the other at each coordinate as:

$$\Delta d_{\text{isotherm}} = d_{\text{steady-state}} - d_{\text{transient}} \tag{11}$$

with $\Delta d_{\text{isotherm}}$ being the difference in depth of the isotherm. This results in positive values when the transient isotherm is shallower than the steady-state isotherm (Figures 4c, 4d, 5c, and 5d).

The resulting profiles of $\Delta d_{\text{isotherm}}$ for the different extension velocities in narrow and wide rift settings are shown in Figures 4c, 4d, 5c, and 5d, respectively. For narrow rift settings, the evolving low topographical

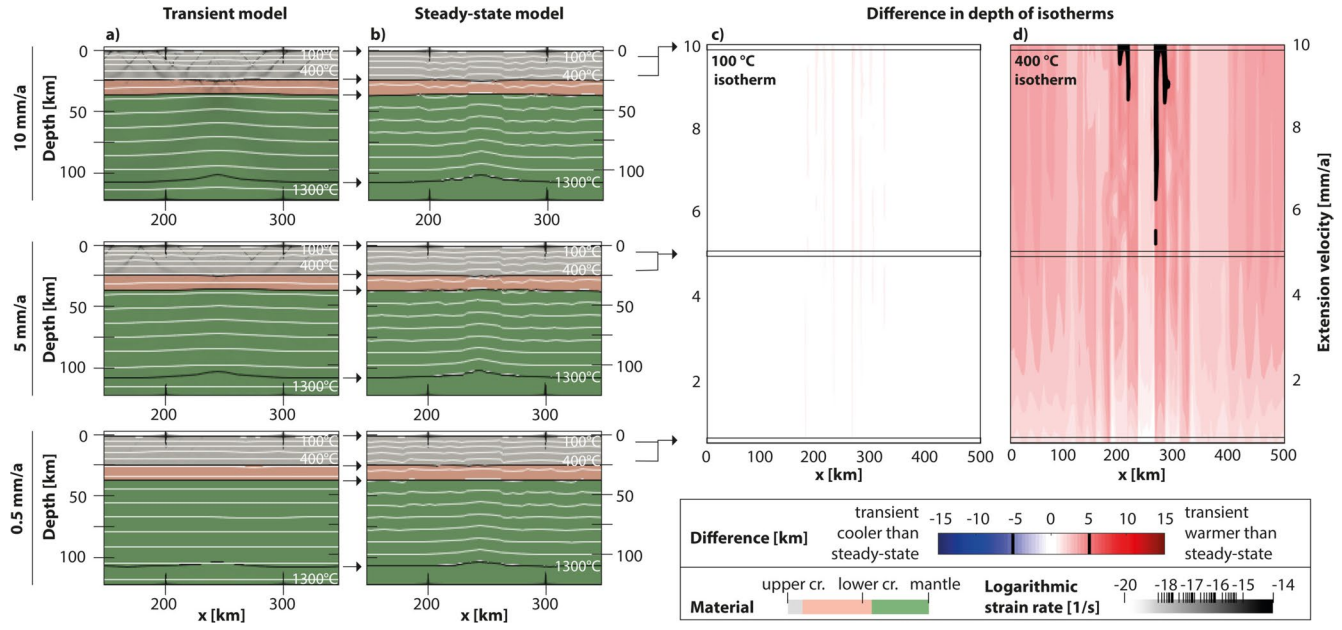

Figure 5. Left: Profiles of three exemplary **wide rift models** with an initial crustal thickness of 40 km and different extension velocities (of 0.5, 5 and 10 mm/a, respectively). (a) The thermal, compositional, and deformation structure of the transient model at 50 km of total extension and (b) the corresponding steady-state model. Colors indicate the different materials of the model as given in Figure 3 and Table 2. The strain rate is superposed in a transparent gray scale. White lines mark the depths of isotherms with a spacing of 100°C. Black arrows between (a) and (b) point at the material contours that are extracted from the transient models to define the material structure of the steady-state models. **Right:** Influence of the extension velocity on the difference between transient and steady-state models. Differences between transient and steady-state models are color-coded in terms of the respective $\Delta d_{\text{isotherm}}$ of (c) the 100°C isotherm and (d) the 400°C isotherm. Red colors indicate a warmer crust in the transient model with the isotherms being shallower compared to the steady-state model. The black contour marks a 5 km difference in depth.

elevations determine the width of the overall positive values of $\Delta d_{\text{isotherm}}$ across the rift valley (Figures 4c and 4d). The 1D steady-state heat equation (Equation 10) generates a relatively regular isotherm spacing between surface and LAB, which leads to deeper crustal steady-state isotherms below low topographical elevations. In the rift center, the topographical effect is counteracted by the elevated LAB, which moves the steady-state isotherms upwards making them more similar to the shallowly advected transient isotherms and hence reduces values for $\Delta d_{\text{isotherm}}$. Contrarily, the maximum $\Delta d_{\text{isotherm}}$ is situated beneath the sides of the rift valley where the LAB is less elevated, but where the topography is small. Here, the transient isotherms still show an advection component while the relatively large distance between the surface and the LAB increases the spacing between steady-state isotherms, which moves them deeper into the crust. The calculated maximum $\Delta d_{\text{isotherm}}$ of the 100°C isotherm is less than 5 km, but exceeds 10–15 km for the 400°C isotherm for rifts faster than 1 mm/a. Wide rift settings, in contrast, lack a strong topographical relief, and also the LAB is elevated only modestly across a wide region (Figures 5a and 5b). This results in a more homogeneous distribution of values for $\Delta d_{\text{isotherm}}$ over the entire model width. The horst and graben topography nonetheless manifests as alternating values for $\Delta d_{\text{isotherm}}$ along the x-axis, that, however, exceed 5 km only locally.

We employ standard statistics in order to quantify the first-order thermal transient effects for all configurations (Figure 6). To this aim, the arithmetic mean and standard deviation of the absolute differences in isotherm depth $\Delta d_{\text{isotherm}}$ are calculated over all x-coordinates extracted from the central third of each model, which is where most surface deformation localizes for narrow rifts. The smaller the arithmetic mean and the standard deviation envelope, the more similar are the isotherm depths of a transient and corresponding steady-state model and thus the smaller is the transient signal. We therefore propose the concept of a similarity threshold ϵ. If the absolute difference in depth is smaller than ϵ, the analyzed set of models can be considered in thermal steady-state within the given assumptions of ϵ. We employ exemplary ϵ values of ± 2.5 and ± 5 km, which lie in the range of uncertainties of geophysical data interpretations at crustal depths. However, when evaluating LAB depths, these numbers could also be chosen significantly higher as

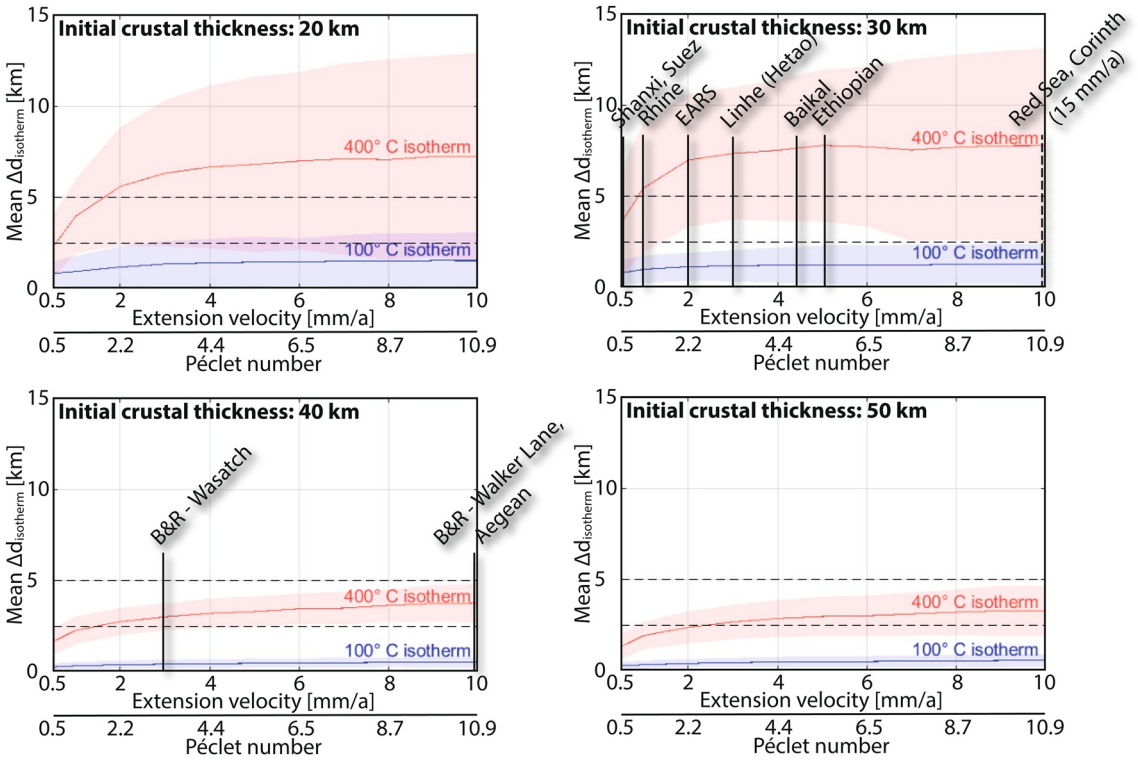

Figure 6. Mean differences of the isotherm depth after 50 km of extension as obtained from the central third of the model domain, which includes the entire rift region for all narrow rifts. Each image shows results for a different initial crustal thickness. The *x*-axis indicates both the extension velocity in mm/a and the corresponding Péclet number as calculated from the parameters at the start of each model (Equation 9). Solid lines give the arithmetic mean of the deviation in the central third of the model. The one standard deviation interval is shown as a colored envelop. Examples of modern rifts are plotted for comparison, references for extension velocities are listed in Table 1 and locations are shown in Figure 1. The dashed lines represent the similarity thresholds $\epsilon = \pm 2.5$ and $\epsilon = \pm 5$ km. B&R, Basin and Range; EARS, East African Rift System.

the uncertainty of the thickness of the lithosphere may be >10–20 km depending on the database and LAB definition used (e.g., Eaton et al., 2009; Fischer et al., 2010). We therefore emphasize that the values for ϵ used here are exemplary and should be adjusted to the purpose of specific studies and data uncertainties. Depending on the resolution of the problem, ϵ can be applied both to the arithmetic mean along the entire profile (Figure 6) and to a single *x*-location (Figures 4c, 4d, 5c, and 5d).

According to this workflow, we find that a steady-state modeling approach is not appropriate for:

(1) The 100°C isotherm in a narrow rift setting for extension velocities >0.5 mm/a, as the maximum $\Delta d_{\text{isotherm}}$ beneath the sides of the rift valley exceeds the similarity threshold $\epsilon = \pm 2.5$ km for 20–30 km of initial crustal thickness (Figure 4c).
(2) The 400°C isotherm in a narrow rift setting regardless of the magnitude of the extension velocity and the initial crustal thickness, if $\epsilon = \pm 2.5$ km is used. For extension velocities >1 mm/a and 20 km of initial crustal thickness as well as for >0.5 mm/a and 30 km initial crustal thickness, the arithmetic mean $\Delta d_{\text{isotherm}}$ exceeds even $\epsilon = \pm 5$ km (Figure 6). The maximum $\Delta d_{\text{isotherm}}$ beneath the sides of the rift valley reaches values of 10–17 km (Figure 4d).
(3) The 400°C isotherm in a wide rift setting where certain extension velocities occur: The arithmetic mean $\Delta d_{\text{isotherm}}$ exceeds $\epsilon = \pm 2.5$ km for extension velocities of >1 mm/a and >2 mm/a for initial crustal thicknesses of 40 and 50 km, respectively (Figure 6). Beneath the sides of the rift valley, the maximum $\Delta d_{\text{isotherm}}$ exceeds $\epsilon = \pm 5$ km for extension velocities of >5 mm/a (Figure 5d).

We furthermore consistently find that the mean $\Delta d_{\text{isotherm}}$ increases with extension velocity for all initial crustal thicknesses (Figure 6). The mean $\Delta d_{\text{isotherm}}$ first increases rapidly for extension velocities <2 mm/a while the curve flattens, but continues to increase for extension velocities >2 mm/a. For fast extending

narrow rifts, the mean $\Delta d_{\text{isotherm}}$ reaches up to 1.5 and 7.5 km for the 100°C and 400°C isotherm, respectively. For wide rifts the mean $\Delta d_{\text{isotherm}}$ amounts to 0.5 and 4 km for the 100°C and 400°C isotherm, respectively.

4. Discussion

In the following section, we first explore how present-day continental rifts compare to our generic findings. We then highlight implications and limitations of our models and explain the choice of the snapshot at 50 km of extension for thermal comparison. Finally, we discuss alternative ways to setup the steady-state models and to represent thermal steady-stateness.

In Figure 6, we assess the first-order thermal steady-stateness of natural rifts by mapping the associated divergence rate onto the diagram for the initial crustal thickness. Taking the Baikal Rift in the upper right panel as an example, it can be seen that the mean $\Delta d_{\text{isotherm}}$, the mean deviation of the steady-state from the transient models, for the modeled temperature of 400°C (red) exceeds both considered values of the similarity threshold ϵ (horizontal dashed lines). This means that according to the approach presented in this study, the Baikal Rift cannot be assumed in thermal steady-state for intermediate crustal temperatures. Contrarily, the mean $\Delta d_{\text{isotherm}}$ for 100°C (blue) is situated below both exemplary values for ϵ and can hence be considered suitable for a steady-state modeling approach (– to assess $\Delta d_{\text{isotherm}}$ at specific x-locations in a rift region, the reader is referred to Figures 4c, 4d, 5c, and 5d).

Subsequently, Figure 6 shows that wide rifts, like the Basin and Range province and the Aegean, as well as slow narrow rifts, like the Shanxi and Suez rifts (0.5 mm/a), are better represented by a steady-state model than faster narrow rifts, like the African rifts or the Gulf of Corinth. However, even for an extension velocity of 0.5 mm/a, the maximum $\Delta d_{\text{isotherm}}$ for the shallow 100°C isotherm exceeds $\epsilon = \pm 2.5$ km locally, beneath the sides of the rift valley. The average $\Delta d_{\text{isotherm}}$ for 1 mm/a (e.g., Rhine graben) already exceeds $\epsilon = \pm 5$ km. The use of a thermal steady-state model for narrow rifts would thus introduce large uncertainties.

To further demonstrate the implications of these results, we consider a slow rift with an extension velocity of 1 mm/a and 30 km initial crustal thickness, which is similar to the Rhine graben. For this rift, the transient model predicts a temperature of around 450°C for a point at 20 km depth beneath the rift center. However, in the steady-state model, it is 20°C colder at that location. Beneath the sides of the rift valley, where the maximum $\Delta d_{\text{isotherm}}$ is located, a point at 20 km depth would be even 150°C colder in a steady-state model compared to a transient model. In terms of depth, maximum values of $\Delta d_{\text{isotherm}}$ reach 10–17 km for the 400°C isotherm, which is in the range of the actual 400°C isotherm depth in a typical continental setting: A temperature gradient of 25°C/km and 0°C at the surface implies a depth of 16 km for 400°C to occur. This means that in fast narrow rifts that feature a pronounced transient tectonic temperature component and therewith elevated temperature gradients, the introduced uncertainty might even be a multiple of the actual isotherm depth—a temperature gradient of 100°C/km and 0°C at the surface leads to a depth of 4 km for 400°C compared to maximum values of $\Delta d_{\text{isotherm}}$ of 10–17 km.

Errors introduced by neglecting transient thermal processes do not only affect models that directly assess the temperature distribution. They also impact other derived variables, as many physical and chemical processes as well as rock properties are temperature dependent. Ignoring the transients in the thermal field would for example change the estimated rheological behavior by assuming a wider domain of brittle deformation inside the rift valley due to lower crustal temperatures. Whenever considering the thermal field to be in equilibrium, our analysis can be used to estimate the uncertainty that is introduced into the model. In this study, we chose a continental rift setting, but large-scale transient thermal signals can also be expected in other tectonically active regions, for example, around orogenic belts (Meeßen, 2019).

Our modeling approach focuses on first-order rift dynamics and accordingly includes several limitations. First of all, our models are two-dimensional. This is justified by the fact that rift segments are geometrically continuous in the rift-parallel direction, which is why major along-strike variations of the thermal field are not expected. For simplicity, we do not include second-order complexities such as magmatic activity, the influence of plumes, the thermal blanketing by a sedimentary cover or underground water circulation and mineral reactions (e.g., Bousquet et al., 2005; Hacker et al., 2003; Koptev et al., 2018; Oliva et al., 2019; Scheck-Wenderoth & Maystrenko, 2013; Scheck-Wenderoth et al., 2014). The models furthermore consist of

four homogeneous layers (upper crust, lower crust, lithospheric mantle, asthenosphere) that do not account for potential spatial variability of thermal properties as these models are not designed to reflect a specific real-world example, but to generically investigate the process of isotherm advection during continental rifting. Fully aware of these simplifications, the so obtained dynamic models are taken as generalized analogs for a rift-typical tectonothermal history which is disregarded by steady-state approaches for thermal field modeling.

So far we presented the tectonothermal signal of all models after a fixed amount of 50 km of extension, even though we performed the analysis continuously until reaching 100 km of accumulated extension. When applying the workflow stepwise to other finite extension values and analyzing the variability of steady-stateness, we find the following general temporal development of mean $\Delta d_{\text{isotherm}}$ (Figure S4): after a build-up phase, the general order of magnitude of the mean $\Delta d_{\text{isotherm}}$ first remains constant before decreasing slightly. This decrease corresponds to a closer approximation of the steady-state models to the transient ones. Considering an exemplary model with an initial crustal thickness of 30 km and an extension velocity of 3 mm/a, the decrease amounts to 2 km (Figure S4 upper left). Its onset varies according to extension velocity: for slowly and moderately extending rifts it occurs after 50–70 km of extension, while manifesting a few tens of kilometers of extension later for faster rifts. Tectonically, the decrease coincides with a change in border fault geometry, which has previously been described as the transition from stretching to thinning mode during rift evolution (Chenin et al., 2018; Lavier & Manatschal, 2006). Our modeling suite thus shows that steady-state thermal models become closer to their transient equivalents during the rift episode when the deformation style changes. In line with this finding, to obtain an estimate for a maximum error potentially introduced in steady-state models, we base the steady-state assessment on the evolutionary snapshots at 50 km of extension, where all models are close to the maximum $\Delta d_{\text{isotherm}}$ regardless of the extension velocity.

A significant decision for the analysis of this paper is the choice of the workflow to set up the steady-state models, which includes the choice of the parameter that represents the LAB. For better comparability of our results, we designed the steady-state models as similar to data-integrative modeling approaches as possible (Gac et al., 2016; Maystrenko & Gernigon, 2018; Tesauro et al., 2012). We have used snapshots of the deep structural configuration of the transient models as the counterpart to the LAB depth that is derived from temperature conversions of seismic tomography studies and used as lower boundary conditions of data-integrative thermal models. Alternatively to those models presented in Figures 4–6 that are based on the extracted material contour at the bottom of the lithosphere, a calculation of the steady-state models can also be based on the 1300°C isotherm as extracted from the transient model. Taking the transient 1300°C isotherm as the new thermal LAB for the steady-state models may seem to be the more direct approach, but it has the disadvantage that its geometrical evolution is significantly affected by the predefined initial vertical model size through thermal boundary conditions. On the other hand, our approach of converting a material discontinuity into an isotherm could also be questioned, but as its evolution is independent of the model size, we regard it as the more appropriate lower boundary condition for later snapshots. We tested the impact of both possibilities and despite the fundamental differences in the nature of the two approaches, we find that both lead to qualitatively similar results, proving our findings regarding the influence of the initial crustal thickness and extension velocity on the steady-stateness of transient systems (compare Figures 4–6 to Figures S1–S3). The choice of 1300°C as the absolute model temperature at the LAB lies within the range of other lithospheric-scale models (Afonso et al. (2016): 1250°C, Balling et al. (2013): 1300°C, Carballo et al. (2015): 1330°C, Sippel et al. (2017): 1350°C). In Figure S6 we show that the overall pattern of $\Delta d_{\text{isotherm}}$ remains comparable when using 1250°C as the temperature at the LAB.

An important finding of this study is that the discussed steady-state isotherms of 100°C and 400°C are almost everywhere deeper than the corresponding transient isotherms, independently of the representation of the LAB. This is due to the upward advection of hot material in a rift setting. Both sets of steady-state models are consistent in this point, regardless of whether a material LAB contour or an associated isotherm is extracted from the transient model (compare Figures S1–S3 in the supplement to Figures 4–6). However, when the 1300°C isotherm is extracted from a transient model, the values for $\Delta d_{\text{isotherm}}$ are larger, influence a wider rift domain and affect more rift-distant locations than for the case of a material discontinuity. This is because the 1300°C isotherm of a transient model is generally not as elevated as the lower boundary of the

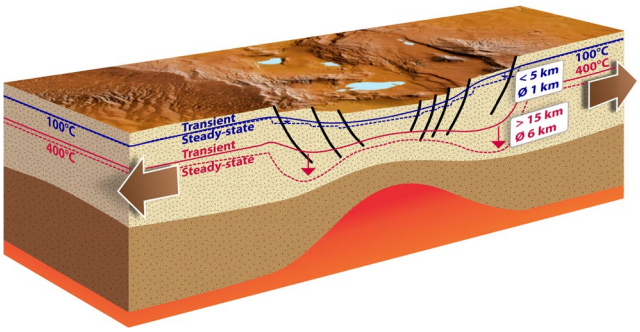

Figure 7. A cartoon of a continental narrow rift with sketches of faults in black (not to scale). The blue and red lines show the generalized main trends and features of the 100°C and 400°C isotherms of the narrow rift transient models (solid lines) and the corresponding steady-state models (dashed lines). The results suggest that isotherms from steady-state models are deeper than those from the corresponding transient models. The maximum difference for the 100°C isotherm is less than 5 km, but more than 10–15 km for the 400°C isotherm for rifts faster than 1 mm/a. Mean values for the thermal model difference are 1–1.5 and 6 km, respectively.

modeled compositional unit of the lithospheric mantle. Associated crustal steady-state isotherms hence remain deeper within the subsurface, which contrasts the corresponding transient isotherms that are further moved to shallow depths by advective material transport. Accordingly, the values for $\Delta d_{\text{isotherm}}$ increase. The difference of the two sets of models is especially important for slower rifts, as for faster rifts the 1300°C isotherm coincides better with the material discontinuity at the base of the lithosphere.

For both definitions of the LAB, the values for $\Delta d_{\text{isotherm}}$ increase with increasing extension velocity. The results hence show the expected positive relationship between $\Delta d_{\text{isotherm}}$ and the extension velocity. This is readily explained by faster advection of hot material for higher extension velocities, a process that dominates over the counteracting heat conduction that would re-equilibrate temperatures. This effect can also be seen in the Péclet numbers associated with the extension velocities. With the extension velocities of 0.5–10 mm/a, our models span the entire transition between predominantly conductive heat transport ($Pe < 1$) and predominantly advective heat transport ($Pe > 10$) (Sandiford, 2002), see Figure 6. This change in heat transport mechanism is reflected in the values for $\Delta d_{\text{isotherm}}$ that increase the more important heat advection becomes. However, our results show that Péclet numbers alone are too general to decide about the validity of the steady-state assumption as this also depends to a large degree on the structure of the rift, that is, whether it classifies as narrow or wide rift type.

We translate the importance of heat advection into a threshold-based approach to represent thermal steady-stateness. Hence a temperature field from a dynamic model can be considered in steady-state when $\Delta d_{\text{isotherm}}$ is smaller than a given similarity threshold ϵ. An alternative approach would be to assess the change of a certain parameter of the evolution models over time such as the temperature at depth. However, this would still require the introduction of a threshold, for example, the temperature change through time as a percentage of actual temperatures as in Peacock (1996) for subduction settings. By comparing transient models to steady-state models with the same material configuration, we stay closer to the setup of published lithospheric-scale thermal models and provide a reference basis for the development of this kind of models in the future.

5. Conclusion

Using numerical modeling, we investigate the validity of the thermal steady-state assumption in extensional continental settings. We show that neglecting tectonic transient thermal effects yields a systematic error in terms of the depth of crustal isotherms. Since these isotherms are advected upwards during rifting, they are always shallower than predicted by the steady-state assumption. For higher extension velocities, this process becomes more important and affects larger depths.

We find that wide rifts reside close to thermal steady-state even for relatively high extension velocities. For narrow rifts, however, we find a speed limit of roughly 0.5–2 mm/a for the applicability of the steady-state assumption. Thus, not only relatively fast rifts like the Main Ethiopian Rift, the Afar rift segments, the Red Sea, and the Gulf of Corinth, but even slow rifts like the Kenya Rift, the Rhine Graben, and Rio Grande Rift must be expected to feature a pronounced transient component in the temperature field and to therefore violate the thermal steady-state assumption for deeper crustal isotherms.

We furthermore illustrate that the speed limit depends on the exact depth and location studied. This is due to the fact that isotherms in steady-state models strongly follow the surface topography and the depth of the LAB, which results in a maximum difference between transient and steady-state models adjacent to the high topography of the rift shoulders. The influence of the thermal boundary conditions varies with depth and we therefore find that the steady-stateness of a model depends on the considered isotherm (Figure 7). Where shallow isotherms are investigated (e.g., the 100°C isotherm), the transient imprint of rifting appears

to be negligible. Contrarily, steady-state assessments of intermediate isotherms (e.g., the 400°C isotherm) systematically lead to underestimations of crustal temperatures especially for narrow rift settings.

In light of these findings, our work does not only put a speed limit on the thermal steady-state assumption, but also provides a way to include the tectonothermal signal as an uncertainty range. This is especially useful for settings where there is no alternative to a steady-state modeling approach.

Data Availability Statement

The specific version of the geodynamic modeling software ASPECT that was used in this study [Advanced Solver for Problems in Earth's ConvecTion, version 2.0.0-pre with deal.II version 8.5.1] is available from the Zenodo repository with the https://doi.org/10.5281/zenodo.3778176. This study was conducted within the Helmholtz Young Investigators Group CRYSTALS (VH-NG-1132).

Acknowledgments
We are grateful for the detailed and constructive comments of J. C. Afonso and an unknown reviewer that substantially helped to improve the manuscript. This study was conducted within the Helmholtz Young Investigators Group CRYSTALS (VH-NG-1132). We thank the Computational Infrastructure for Geodynamics (geodynamics.org) which is funded by the National Science Foundation under award EAR-0949446 and EAR-1550901 for supporting the development of ASPECT. Computations were performed on GFZ clusters and on Konrad, an HLRN cluster facility. Figures in this paper were made with ParaView, InkScape and Adobe Illustrator.

References

Afonso, J. C., Moorkamp, M., & Fullea, J. (2016). *Imaging the lithosphere and upper mantle. In Integrated imaging of the earth* (pp. 191–218). American Geophysical Union (AGU). Retrieved from https://agupubs.onlinelibrary.wiley.com/doi/abs/10.1002/9781118929063.ch10

Afonso, J. C., & Ranalli, G. (2004). Crustal and mantle strengths in continental lithosphere: Is the jelly sandwich model obsolete? *Tectonophysics*, *394*(3), 221–232. https://doi.org/10.1016/j.tecto.2004.08.006

Agemar, T., Alten, J.-A., Ganz, B., Kuder, J., Kuehne, K., Schumacher, S., & Schulz, R. (2014). The Geothermal Information System for Germany—GeotIS. *Zeitschrift Der Deutschen Gesellschaft Fur Geowissenschaften*, *165*(2), 129–144. (Place: Stuttgart Publisher: E Schweizerbartsche Verlagsbuchhandlung WOS:000338489200005). https://doi.org/10.1127/1860-1804/2014/0060

Armitage, J. J., Petersen, K. D., & Pérez-Gussinyé, M. (2018). The role of crustal strength in controlling magmatism and melt chemistry during rifting and breakup. *Geochemistry, Geophysics, Geosystems*, *19*(2), 534–550. https://doi.org/10.1002/2017GC007326

Arndt, D., Bangerth, W., Davydov, D., Heister, T., Heltai, L., Kronbichler, M., et al. (2017). The deal.II library, version 8.5. *Journal of Numerical Mathematics*, *25*(3), 137–145. Retrieved from https://www.degruyter.com/view/j/jnma.2017.25.issue-3/jnma-2017-0058/jnma-2017-0058.xml

Artemieva, I. M. (2006). Global 1°x1° thermal model TC1 for the continental lithosphere: Implications for lithosphere secular evolution. *Tectonophysics*, *416*(1), 245–277. https://doi.org/10.1016/j.tecto.2005.11.022

Artemieva, I. M. (2009). The continental lithosphere: Reconciling thermal, seismic, and petrologic data. *Lithos*, *109*(1), 23–46. https://doi.org/10.1016/j.lithos.2008.09.015

Balling, P., Maystrenko, Y., & Scheck-Wenderoth, M. (2013). The deep thermal field of the Glueckstadt Graben. *Environmental Earth Sciences*, *70*(8), 3505–3522. https://doi.org/10.1007/s12665-013-2750-z

Bangerth, W., Dannberg, J., Gassmoeller, R., Heister, T., Austermann, J., Fraters, M., & Glerum, A. (2018). *ASPECT v2.0.0 [software]*. https://doi.org/10.5281/zenodo.1244587

Bayer, U., Scheck, M., & Koehler, M. (1997). Modeling of the 3d thermal field in the northeast German basin. *Geologische Rundschau*, *86*(2), 241–251. https://doi.org/10.1007/s005310050137

Bendick, R., McClusky, S., Bilham, R., Asfaw, L., & Klemperer, S. (2006). Distributed Nubia–Somalia relative motion and dike intrusion in the main Ethiopian rift. *Geophysical Journal International*, *165*(1), 303–310. https://doi.org/10.1111/j.1365-246X.2006.02904.x

Bennett, R. A., Wernicke, B. P., & Davis, J. L. (1998). Continuous GPS measurements of contemporary deformation across the northern basin and range province. *Geophysical Research Letters*, *25*(4), 563–566. https://doi.org/10.1029/98GL00128

Berglund, H. T., Sheehan, A. F., Murray, M. H., Roy, M., Lowry, A. R., Nerem, R. S., & Blume, F. (2012). Distributed deformation across the Rio Grande rift, great plains, and Colorado Plateau. *Geology*, *40*(1), 23–26. https://doi.org/10.1130/G32418.1

Bousquet, R., Goffé, B., Le Pichon, X., de Capitani, C., Chopin, C., & Henry, P. (2005). Comment on "Subduction factory: 1. Theoretical mineralogy, densities, seismic wave speeds, and H_2O contents" by Bradley R. Hacker, Geoffrey A. Abers, and Simon M. Peacock: COMMENTARY. *Journal of Geophysical Research*, *110*(B2). https://doi.org/10.1029/2004JB003450

Braun, J., & Beaumont, C. (1989). A physical explanation of the relation between flank uplifts and the breakup unconformity at rifted continental margins. *Geology*, *17*(8), 760–764. https://doi.org/10.1130/0091-7613(1989)017⟨0760:APEOTR⟩2.3.CO;2

Braun, J., Beek, P. V. D., & Batt, G. (2006). *Quantitative thermochronology: Numerical methods for the interpretation of thermochronological data*. Cambridge University Press. https://doi.org/10.1017/CBO9780511616433

Brun, J. P., Gutscher, M. A., & dekorp-ecors teams. (1992). Deep crustal structure of the Rhine Graben from DEKORP-ECORS seismic reflection data: A summary. *Tectonophysics*, *208*(1), 139–147. https://doi.org/10.1016/0040-1951(92)90340-C

Brun, J.-P., & Sokoutis, D. (2018). Core complex segmentation in North Aegean, A dynamic view. *Tectonics*, *37*(6), 1797–1830. https://doi.org/10.1029/2017TC004939

Brune, S. (2014). Evolution of stress and fault patterns in oblique rift systems: 3-d numerical lithospheric-scale experiments from rift to breakup. *Geochemistry, Geophysics, Geosystems*, *15*(8), 3392–3415. https://doi.org/10.1002/2014GC005446

Brune, S., Heine, C., Clift, P. D., & Pérez-Gussinyé, M. (2017). Rifted margin architecture and crustal rheology: Reviewing Iberia–Newfoundland, Central South Atlantic, and South China Sea. *Marine and Petroleum Geology*, *79*, 257–281. https://doi.org/10.1016/j.marpetgeo.2016.10.018

Brune, S., Heine, C., Pérez-Gussinyé, M., & Sobolev, S. V. (2014). Rift migration explains continental margin asymmetry and crustal hyper-extension. *Nature Communications*, *5*(1), 1–9. https://doi.org/10.1038/ncomms5014

Buck, W. R. (1991). Modes of continental lithospheric extension. *Journal of Geophysical Research*, *96*(B12), 20161–20178. Retrieved from https://agupubs.onlinelibrary.wiley.com/doi/abs/10.1029/91JB01485

Burov, E. B. (2011). Rheology and strength of the lithosphere. *Marine and Petroleum Geology*, *28*(8), 1402–1443. https://doi.org/10.1016/j.marpetgeo.2011.05.008

Calais, E., Lesne, O., Déverchère, J., San'kov, V., Lukhnev, A., Miroshnitchenko, A., et al. (1998). Crustal deformation in the Baikal Rift from GPS measurements. *Geophysical Research Letters*, *25*(21), 4003–4006. https://doi.org/10.1029/1998GL900067

Carballo, A., Fernandez, M., JimCarballonez-Munt, I., Torne, M., VergCarballos, J., Melchiorre, M., et al. (2015). From the North-Iberian margin to the Alboran basin: A lithosphere geo-transect across the Iberian plate. *Tectonophysics*, *663*, 399–418. https://doi.org/10.1016/j.tecto.2015.07.009

Chapman, D. S. (1986). Thermal gradients in the continental crust. *Geological Society, London, Special Publications*, *24*(1), 63–70. https://doi.org/10.1144/GSL.SP.1986.024.01.07

Chenin, P., Schmalholz, S. M., Manatschal, G., & Duretz, T. (2020). Impact of crust-mantle mechanical coupling on the topographic and thermal evolutions during the necking phase of 'magma-poor' and 'sediment-starved' rift systems: A numerical modeling study. *Tectonophysics*, *786*, 228472. https://doi.org/10.1016/j.tecto.2020.228472

Chenin, P., Schmalholz, S. M., Manatschal, G., & Karner, G. D. (2018). Necking of the lithosphere: A reappraisal of basic concepts with thermo-mechanical numerical modeling. *Journal of Geophysical Research: Solid Earth*, *123*(6), 5279–5299. https://doi.org/10.1029/2017JB014155

Corti, G., Molin, P., Sembroni, A., Bastow, I. D., & Keir, D. (2018). Control of pre-rift lithospheric structure on the architecture and evolution of continental rifts: Insights from the main Ethiopian rift, East Africa. *Tectonics*, *37*(2), 477–496. https://doi.org/10.1002/2017TC004799

Davies, D. R., Le Voci, G., Goes, S., Kramer, S. C., & Wilson, C. R. (2016). The mantle wedge's transient 3-d flow regime and thermal structure. *Geochemistry, Geophysics, Geosystems*, *17*(1), 78–100. https://doi.org/10.1002/2015GC006125

Duclaux, G., Huismans, R. S., & May, D. (2018). *Rotation, narrowing and preferential reactivation of brittle structures during oblique rifting. EGU General Assembly Conference Abstracts* (p. 7247). Retrieved from https://ui.adsabs.harvard.edu/abs/2018EGUGA.20.7247D/abstract

Duretz, T., Petri, B., Mohn, G., Schmalholz, S. M., Schenker, F. L., & Müntener, O. (2016). The importance of structural softening for the evolution and architecture of passive margins. *Scientific Reports*, *6*(1), 1–7. https://doi.org/10.1038/srep38704

Eaton, D. W., Darbyshire, F., Evans, R. L., Grütter, H., Jones, A. G., & Yuan, X. (2009). The elusive lithosphere-asthenosphere boundary (LAB) beneath cratons. *Lithos*, *109*(1), 1–22. https://doi.org/10.1016/j.lithos.2008.05.009

Ebinger, C., & Scholz, C. A. (2012). *Continental rift basins: The East African perspective. In Tectonics of sedimentary basins* (pp. 183–208). John Wiley & Sons, Ltd. https://doi.org/10.1002/9781444347166.ch9

Ehlers, T. A., & Farley, K. A. (2003). Apatite (u–th)/he thermochronometry: Methods and applications to problems in tectonic and surface processes. *Earth and Planetary Science Letters*, *206*(1), 1–14. https://doi.org/10.1016/S0012-821X(02)01069-5

Fischer, K. M., Ford, H. A., Abt, D. L., & Rychert, C. A. (2010). The lithosphere-asthenosphere boundary. *Annual Review of Earth and Planetary Sciences*, *38*(1), 551–575. https://doi.org/10.1146/annurev-earth-040809-152438

Freymark, J., Sippel, J., Scheck-Wenderoth, M., Bär, K., Stiller, M., Fritsche, J.-G., & Kracht, M. (2017). The deep thermal field of the Upper Rhine Graben. *Tectonophysics*, *694*, 114–129. https://doi.org/10.1016/j.tecto.2016.11.013

Fullea, J., Afonso, J. C., Connolly, J. A. D., Fernández, M., García-Castellanos, D., & Zeyen, H. (2009). LitMod3d: An interactive 3-d software to model the thermal, compositional, density, seismological, and rheological structure of the lithosphere and sublithospheric upper mantle. *Geochemistry, Geophysics, Geosystems*, *10*(8). https://doi.org/10.1029/2009GC002391

Fullea, J., Lebedev, S., Agius, M. R., Jones, A. G., & Afonso, J. C. (2012). Lithospheric structure in the Baikal–central Mongolia region from integrated geophysical-petrological inversion of surface-wave data and topographic elevation. *Geochemistry, Geophysics, Geosystems*, *13*(8). https://doi.org/:10.1029/2012GC004138

Gac, S., Klitzke, P., Minakov, A., Faleide, J. I., & Scheck-Wenderoth, M. (2016). Lithospheric strength and elastic thickness of the Barents Sea and Kara Sea region. *Tectonophysics*, *691*, 120–132. https://doi.org/10.1016/j.tecto.2016.04.028

Gawthorpe, R. L., Leeder, M. R., Kranis, H., Skourtsos, E., Andrews, J. E., Henstra, G. A., et al. (2018). Tectono-sedimentary evolution of the Plio-Pleistocene Corinth rift, Greece. *Basin Research*, *30*(3), 448–479. https://doi.org/10.1111/bre.12260

Glerum, A., Thieulot, C., Fraters, M., Blom, C., & Spakman, W. (2018). Nonlinear viscoplasticity in ASPECT: Benchmarking and applications to subduction. *Solid Earth*, *9*(2), 267–294. https://doi.org/10.5194/se-9-267-2018

Golombek, M. P., McGill, G. E., & Brown, L. (1983). Tectonic and geologic evolution of the Espanola basin, Rio Grande rift: Structure, rate of extension, and relation to the state of stress in the western United States. *Tectonophysics*, *94*(1), 483–507. https://doi.org/10.1016/0040-1951(83)90031-8

Gudmundsson, J.-S. (1988). The elements of direct uses. *Geothermics*, *17*(1), 119–136. https://doi.org/10.1016/0375-6505(88)90009-0

Guillou-Frottier, L., Buttles, J., & Olson, P. (1995). Laboratory experiments on the structure of subducted lithosphere. *Earth and Planetary Science Letters*, *133*(1), 19–34. https://doi.org/10.1016/0012-821X(95)00045-E

Hacker, B. R., Abers, G. A., & Peacock, S. M. (2003). Subduction factory 1. Theoretical mineralogy, densities, seismic wave speeds, and H_2O contents. *Journal of Geophysical Research*, *108*(B1). https://doi.org/10.1029/2001JB001127

Hamilton, W. (1987). Crustal extension in the Basin and Range Province, southwestern United States. *Geological Society, London, Special Publications*, *28*(1), 155–176. https://doi.org/10.1144/GSL.SP.1987.028.01.12

Hammond, W. C., & Thatcher, W. (2004). Contemporary tectonic deformation of the basin and range province, western United States: 10 years of observation with the global positioning system. *Journal of Geophysical Research*, *109*. https://doi.org/10.1029/2003JB002746

Hart, N. R., Stockli, D. F., Lavier, L. L., & Hayman, N. W. (2017). Thermal evolution of a hyperextended rift basin, Mauleon Basin, Western Pyrenees. *Tectonics*, *36*(6), 1103–1128. Retrieved from https://agupubs.onlinelibrary.wiley.com/doi/abs/10.1002/2016TC004365

Heckenbach, E. L., Norden, B., & Fuchs, S. (2019). Evaluation of the glacial impact on the shallow heat-flow density in the North German Basin. In Geophysical Research Abstracts (Vol. 21, EGU2019-12927-1). General Assembly European Geosciences Union, Vienna. Retrieved from https://gfzpublic.gfz-potsdam.de/pubman/faces/ViewItemOverviewPage.jsp?itemId=item_4924897

Heister, T., Dannberg, J., Gassmöller, R., & Bangerth, W. (2017). High accuracy mantle convection simulation through modern numerical methods. II: Realistic models and problems. *Geophysical Journal International*, *210*(2), 833–851. https://doi.org/10.1093/gji/ggx195

Hirth, G., & Kohlstedt, D. (2004). *Rheology of the upper mantle and the mantle wedge: A view from the experimentalists. In inside the subduction factory* (pp. 83–105). American Geophysical Union (AGU). https://doi.org/10.1029/138GM06

Huismans, R. S., & Beaumont, C. (2003). Symmetric and asymmetric lithospheric extension: Relative effects of frictional-plastic and viscous strain softening. *Journal of Geophysical Research*, *108*(B10). https://doi.org/10.1029/2002JB002026

Huismans, R. S., Buiter, S. J. H., & Beaumont, C. (2005). Effect of plastic-viscous layering and strain softening on mode selection during lithospheric extension. *Journal of Geophysical Research*, *110*. https://doi.org/10.1029/2004JB003114

Jammes, S., & Lavier, L. L. (2016). The effect of bimineralic composition on extensional processes at lithospheric scale. *Geochemistry, Geophysics, Geosystems*, *17*(8), 3375–3392. https://doi.org/10.1002/2016GC006399

Jiménez-Munt, I., Torne, M., Fernàndez, M., Vergés, J., Kumar, A., Carballo, A., & García-Castellanos, D. (2019). Deep seated density anomalies across the Iberia–Africa plate boundary and its topographic response. *Journal of Geophysical Research: Solid Earth*. https://doi.org/10.1029/2019JB018445

Kendall, J.-M., & Lithgow-Bertelloni, C. (2016). Why is Africa rifting? *Geological Society, London, Special Publications*, *420*(1), 11–30. https://doi.org/10.1144/SP420.17

Kogan, L., Fisseha, S., Bendick, R., Reilinger, R., McClusky, S., King, R., & Solomon, T. (2012). Lithospheric strength and strain localization in continental extension from observations of the East African rift. *Journal of Geophysical Research: Solid Earth*, *117*. https://doi.org/10.1029/2011JB008516

Koptev, A., Burov, E., Gerya, T., Le Pourhiet, L., Leroy, S., Calais, E., & Jolivet, L. (2018). Plume-induced continental rifting and breakup in ultra-slow extension context: Insights from 3d numerical modeling. *Tectonophysics*, *746*, 121–137. https://doi.org/10.1016/j.tecto.2017.03.025

Kreemer, C., Blewitt, G., & Hammond, W. C. (2010). Evidence for an active shear zone in Southern Nevada linking the Wasatch fault to the eastern California shear zone. *Geology*, *38*(5), 475–478. https://doi.org/10.1130/G30477.1

Kronbichler, M., Heister, T., & Bangerth, W. (2012). High accuracy mantle convection simulation through modern numerical methods. *Geophysical Journal International*, *191*, 12–29. https://doi.org/10.1111/j.1365-246X.2012.05609.x

Lane, A. C. (1923). Geotherms of Lake Superior copper country. *The Geological Society of America Bulletin*, *34*, 703–720.

Lavier, L. L., & Manatschal, G. (2006). A mechanism to thin the continental lithosphere at magma-poor margins. *Nature*, *440*(7082), 324–328. https://doi.org/10.1038/nature04608

Maystrenko, Y. P., & Gernigon, L. (2018). 3-D temperature distribution beneath the Mid-Norwegian continental margin (the Vøring and Møre basins). *Geophysical Journal International*, *212*(1), 694–724. https://doi.org/10.1093/gji/ggx377

McClusky, S., Reilinger, R., Ogubazghi, G., Amleson, A., Healeb, B., Vernant, P., et al. (2010). Kinematics of the southern red sea–afar triple junction and implications for plate dynamics. *Geophysical Research Letters*, *37*(5). https://doi.org/10.1029/2009GL041127

McQuarrie, N., & Wernicke, B. P. (2005). An animated tectonic reconstruction of southwestern North America since 36 ma. *Geosphere*, *1*(3), 147–172. https://doi.org/10.1130/GES00016.1

Meeßen, C. (2019). *The thermal and rheological state of the northern Argentinian Foreland basins*. Retrieved from https://publishup.uni-potsdam.de/frontdoor/index/index/docId/43994

Naliboff, J. B., Buiter, S. J. H., Péron-Pinvidic, G., Osmundsen, P. T., & Tetreault, J. (2017). Complex fault interaction controls continental rifting. *Nature Communications*, *8*(1), 1–9. https://doi.org/10.1038/s41467-017-00904-x

Oliva, S. J., Ebinger, C. J., Wauthier, C., Muirhead, J. D., Roecker, S. W., Rivalta, E., & Heimann, S. (2019). Insights into fault-magma interactions in an early-stage continental rift from source mechanisms and correlated volcano-tectonic earthquakes. *Geophysical Research Letters*, *46*(4), 2065–2074. https://doi.org/10.1029/2018GL080866

Oskin, M., Stock, J., & Martín-Barajas, A. (2001). Rapid localization of Pacific–North America plate motion in the gulf of California. *Geology*, *29*(5), 459–462. Retrieved from https://pubs.geoscienceworld.org/geology/article/29/5/459/192069/Rapid-localization-of-Pacific-North-America-plate. https://doi.org/10.1130/0091-7613(2001)029⟨0459:RLOPNA⟩2.0.CO;2

Peacock, S. M. (1996). Thermal and petrologic structure of subduction zones. In *Subduction* (pp. 119–133). American Geophysical Union (AGU). https://doi.org/10.1029/GM096p0119

Pourhiet, L. L., Burov, E., & Moretti, I. (2004). Rifting through a stack of inhomogeneous thrusts (the dipping pie concept). *Tectonics*, *23*(4). https://doi.org/10.1029/2003TC001584

Reilinger, R., McClusky, S., Paradissis, D., Ergintav, S., & Vernant, P. (2010). Geodetic constraints on the tectonic evolution of the Aegean region and strain accumulation along the Hellenic subduction zone. *Tectonophysics*, *488*(1), 22–30. https://doi.org/10.1016/j.tecto.2009.05.027

Rey, P. F., Teyssier, C., & Whitney, D. L. (2009). Extension rates, crustal melting, and core complex dynamics. *Geology*, *37*(5), 391–394. https://doi.org/10.1130/G25460A.1

Rose, I., Buffett, B., & Heister, T. (2017). Stability and accuracy of free surface time integration in viscous flows. *Physics of the Earth and Planetary Interiors*, *262*, 90–100. https://doi.org/10.1016/j.pepi.2016.11.007

Rutter, E. H., & Brodie, K. H. (2004). Experimental grain size-sensitive flow of hot-pressed Brazilian quartz aggregates. *Journal of Structural Geology*, *26*(11), 2011–2023. https://doi.org/10.1016/j.jsg.2004.04.006

Rybacki, E., Gottschalk, M., Wirth, R., & Dresen, G. (2006). Influence of water fugacity and activation volume on the flow properties of fine-grained anorthite aggregates. *Journal of Geophysical Research*, *111*. https://doi.org/10.1029/2005JB003663

Sandiford, M. (2002). Low thermal Peclet number intraplate orogeny in central Australia. *Earth and Planetary Science Letters*, *201*(2), 309–320. https://doi.org/10.1016/S0012-821X(02)00723-9

Saria, E., Calais, E., Stamps, D. S., Delvaux, D., & Hartnady, C. J. H. (2014). Present-day kinematics of the East African rift. *Journal of Geophysical Research: Solid Earth*, *119*(4), 3584–3600. https://doi.org/10.1002/2013JB010901

Scheck-Wenderoth, M., Cacace, M., Maystrenko, Y. P., Cherubini, Y., Noack, V., Kaiser, B. O., et al. (2014). Models of heat transport in the Central European Basin System: Effective mechanisms at different scales. *Marine and Petroleum Geology*, *55*, 315–331. (Place: Oxford Publisher: Elsevier Sci Ltd WOS:000338620800022). https://doi.org/10.1016/j.marpetgeo.2014.03.009

Scheck-Wenderoth, M., & Maystrenko, Y. P. (2013). Deep control on shallow heat in sedimentary basins. *Energy Procedia*, *40*, 266–275. Retrieved from http://www.sciencedirect.com/science/article/pii/S1876610213016251

Sdrolias, M., & Müller, R. D. (2006). Controls on back-arc basin formation. *Geochemistry, Geophysics, Geosystems*, *7*(4). Retrieved from https://agupubs.onlinelibrary.wiley.com/doi/abs/10.1029/2005GC001090

Sippel, J., Meeßen, C., Cacace, M., Mechie, J., Fishwick, S., Heine, C., et al. (2017). The Kenya rift revisited: insights into lithospheric strength through data-driven 3-d gravity and thermal modeling. *Solid Earth*, *8*(1), 45–81. https://doi.org/10.5194/se-8-45-2017

Smye, A. J., Lavier, L. L., Zack, T., & Stockli, D. F. (2019). Episodic heating of continental lower crust during extension: A thermal modeling investigation of the Ivrea-Verbano Zone. *Earth and Planetary Science Letters*, *521*, 158–168. Retrieved from http://www.sciencedirect.com/science/article/pii/S0012821X19303486

Stamps, D. S., Flesch, L. M., & Calais, E. (2010). Lithospheric buoyancy forces in Africa from a thin sheet approach. *International Journal of Earth Sciences*, *99*(7), 1525–1533. https://doi.org/10.1007/s00531-010-0533-2

Tesauro, M., Hollenstein, C., Egli, R., Geiger, A., & Kahle, H.-G. (2005). Continuous GPS and broad-scale deformation across the rhine graben and the alps. *International Journal of Earth Sciences*, *94*(4), 525–537. https://doi.org/10.1007/s00531-004-0453-0

Tesauro, M., Kaban, M. K., & Cloetingh, S. A. P. L. (2009). A new thermal and rheological model of the European lithosphere. *Tectonophysics*, *476*(3), 478–495. Retrieved from http://www.sciencedirect.com/science/article/pii/S0040195109004120

Tesauro, M., Kaban, M. K., & Cloetingh, S. A. P. L. (2012). Global strength and elastic thickness of the lithosphere. *Global and Planetary Change*, *90–91*, 51–57. Retrieved from http://www.sciencedirect.com/science/article/pii/S0921818111002220

Tetreault, J. L., & Buiter, S. J. H. (2018). The influence of extension rate and crustal rheology on the evolution of passive margins from rifting to break-up. *Tectonophysics*, *746*, 155–172. Retrieved from http://www.sciencedirect.com/science/article/pii/S0040195117303505

Tissot, B. P., Pelet, R., & Ungerer, P. (1987). Thermal history of sedimentary basins, maturation indices, and kinetics of oil and gas generation. *AAPG Bulletin*, *71*(12), 1445–1466. https://doi.org/10.1306/703C80E7-1707-11D7-8645000102C1865D

Tregoning, P., Lambeck, K., Stolz, A., Morgan, P., McClusky, S. C., Beek, P. V. D., et al. (1998). Estimation of current plate motions in Papua New Guinea from global positioning system observations. *Journal of Geophysical Research*, *103*, 12181–12203. Retrieved from https://agupubs.onlinelibrary.wiley.com/doi/abs/10.1029/97JB03676

Turcotte, D., & Schubert, G. (2014). *Geodynamics*. Cambridge University Press. (Google-Books-ID: heJSAwAAQBAJ).

Ulvrova, M. M., Brune, S., & Williams, S. (2019). Breakup without borders: How continents speed up and slow down during rifting. *Geophysical Research Letters*, *46*(3), 1338–1347. Retrieved from https://agupubs.onlinelibrary.wiley.com/doi/abs/10.1029/2018GL080387, https://agupubs.onlinelibrary.wiley.com/doi/pdf/10.1029/2018GL080387

Zhang, Y. Q., Mercier, J. L., & Vergély, P. (1998). Extension in the graben systems around the ordos (China), and its contribution to the extrusion tectonics of South China with respect to Gobi–Mongolia. *Tectonophysics*, *285*(1), 41–75. Retrieved from http://www.sciencedirect.com/science/article/pii/S0040195197001704